Research Article

Eman Aldosari, Mohamed Rabia*, Hassan A. Ewais, Kenan Song

One-pot synthesis of a network of Mn$_2$O$_3$–MnO$_2$–poly(*m*-methylaniline) composite nanorods on a polypyrrole film presents a promising and efficient optoelectronic and solar cell device

Abstract: A one-pot synthesis approach was employed to create a composite nanorod structure (Mn$_2$O$_3$–MnO$_2$–poly(*m*-methylaniline) or Mn$_2$O$_3$–MnO$_2$–P*m*MA) on a polypyrrole (Ppy) film. Optoelectronic and solar cell thin film devices were constructed using n- and p-type layers of Mn$_2$O$_3$–MnO$_2$–P*m*MA and Ppy, respectively. The optical characteristics of the n-layer, coupled with the morphological behavior of its nanorods, enhance optical absorbance efficiency, reducing the bandgap value to 2.48 eV. The behavior of the optoelectronic device is chiefly determined by the significantly higher current density (J_{ph}) value of 0.017 mA/cm^2 compared to the dark current density (J_o) value of 0.002 mA/cm^2. Additionally, the linear dynamic range is 85 dB, and the noise ratio is 12%. The optimized values for the photosensitivity (R) and detectivity (D) at 340 nm are 0.22 mA W^{-1} and 0.47 × 10^8 Jones, respectively. Even at 540 nm, these values decrease to 0.08 and 0.2 × 10^8 Jones, respectively. For solar cell behavior, the short-circuit current (J_{SC}) and open-circuit voltage (V_{OC}) at 540 nm are determined, yielding values of 0.001 mA/cm^2 and 0.98 V, respectively. The outstanding performance of this optoelectronic device, coupled with its solar cell behavior, positions the thin film material for a dual role in various industrial applications.

Keywords: Mn$_2$O$_3$–MnO$_2$, poly(*m*-methylaniline), polypyrrole, optoelectronic, solar cell, nanocomposite

1 Introduction

Presently, fossil fuels play a vital role in meeting the global demand for electrical energy. However, it is becoming increasingly evident that the world's growing need for electricity is on the verge of surpassing the current output capacity of fossil fuels [1,2]. This impending shortfall raises concerns about the sustainability and adequacy of relying solely on fossil fuels to meet the growing energy requirements. However, the produced gases have far-reaching consequences, affecting both the climate and human health. The implications of these pollutants include adverse impacts on air quality, the exacerbation of climate change, and potential health hazards for human populations [3,4].

The development of new and sustainable energy sources stands out as a pivotal solution to address the pressing issues associated with fossil fuel dependence. This pursuit is driven not only by the need to meet the escalating demand for electricity but also by a broader commitment to mitigate the adverse environmental and health effects associated with conventional energy production. Investing in innovative and eco-friendly energy alternatives provides an opportunity to transition toward a more sustainable and resilient energy landscape called renewable energy.

Conversely, solar cells have gained increasing attention as a prominent form of renewable energy due to their

---

* Corresponding author: Mohamed Rabia, Nanomaterials Science Research Laboratory, Chemistry Department, Faculty of Science, Beni-Suef University, Beni-Suef, 62514, Egypt,
e-mail: mohamedchem@science.bsu.edu.eg
Eman Aldosari: Department of Chemistry, College of Science, King Saud University, P. O. Box 145111, Riyadh, Saudi Arabia,
e-mail: ialdowsary@ksu.edu.sa
Hassan A. Ewais: Chemistry Department, Faculty of Science, King Abdulaziz University, P.O Box 80203, Jeddah, 21589, Saudi Arabia
Kenan Song: The Polytechnic School (TPS), School for Engineering of Matter, Transport and Energy (SEMTE), Ira A. Fulton Schools of Engineering, Arizona State University, Mesa, AZ, 85212, United States of America, e-mail: kenan.song@asu.edu

environmentally friendly nature, cost-effectiveness, potent energy conversion capabilities, and notable performance. In recent times, semiconducting polymeric nanostructures have emerged as a focal point in photocatalytic processes, primarily due to their adjustable bandgap and distinctive optical characteristics. This has led to a surge in interest in studying the potential applications of these nanostructures. Among conducting polymers, polyaniline and its derivatives stand out as exceptional because both oxidation and protonation exert reversible control over its electronic structure and electrical characteristics [5,6]. This unique feature positions polyaniline as a material of considerable interest for potential applications, leveraging a wide spectrum of associated electrical and optical properties. Moreover, the material's outstanding environmental and thermal stability has contributed to its growing prominence. The ease of synthesis and remarkable mechanical strength further enhance its appeal, making polyaniline a versatile candidate for various applications.

Diverse materials have been meticulously developed and applied in solar energy applications, showcasing a broad range of alternatives for improving the efficiency and performance of solar cells. Among these materials, manganese-based oxides, vanadium-based materials, cobalt-based materials, molybdenum-based materials, and polymers and organic compounds are particularly important in the advancement of solar energy technology [7,8]. Previous research has investigated a variety of materials for optoelectronic applications, including metal oxides, nitrides, and carbon-based materials such as CuO nanowires [9], graphene/GaN [10], TiN/TiO_2 [11], PbI_2-5%Ag [12], and Ti3C2 MXenes [13], or organic materials such as graphene/P3HT [14], PBBTPD:Tri-PC61BM [15], and ZnO/P3HT/PEDOT:PSS [16]. In these previous studies, the reported photosensitivity (R) values were generally $0.1\ mA\ W^{-1}$ or even smaller, reaching as low as $10^{-4}\ mA\ W^{-1}$. Despite utilizing complex techniques and high-cost materials, the achieved sensitivity remained limited.

The synthesis of pristine polyaniline is not only straightforward but also lends itself to the production of materials with good electrical and optical properties. These properties, together with the material's robust mechanical strength, make it a compelling choice for a variety of applications [17,18]. The material's remarkable stability in different environmental conditions adds to its attractiveness, further fueling the interest in exploring its potential applications in various fields. Researchers have been investigating the incorporation of polyaniline composites into light sensors, like the polyaniline/cellulose acetate composite with a bandgap of 4.02 eV, and the polyvinyl alcohol/polyaniline composite with a bandgap of 2.71 eV. Despite these efforts, the light-sensing capacities of these materials remain relatively weak, indicating the need

for further improvements to enhance their performance in detecting visible light [19,20]. The use of polyaniline composites in light sensors offers promising prospects due to their unique characteristics, including adjustable bandgaps and conductivity, making them suitable for optoelectronic applications. However, the main challenges involve optimizing these materials to effectively sense visible light. One method to improve the light-sensing capacities of polyaniline composites involves refining their structure to better capture and respond to visible light wavelengths. This might involve adjusting the composition ratios of polyaniline and its substrate materials, as well as exploring new composite combinations to achieve better optical properties. Moreover, enhancing the composite matrix by incorporating additional light-absorbing or sensitizing agents could boost its light-sensing capacities. These additives, such as organic dyes or plasmonic nanoparticles, can extend the composite's absorption range into the visible spectrum and improve its photoconductivity. Another strategy for improvement is optimizing the fabrication process to ensure the uniform dispersion and alignment of composite components, thereby reducing charge carrier recombination and improving overall light sensitivity.

Herein, our current research focuses on the development of a highly sensitive and optically efficient Mn_2O_3–MnO_2–P*m*MA/polypyrrole (Ppy) optoelectronic device that includes a solar cell component capable of detecting light in both the ultraviolet (UV) and visible (Vis) regions. This novel device undergoes testing under diverse light conditions, with calculated values for linear dynamic range (LDR), D, R, J_{SC}, V_{OC}, and noise ratio. These parameters serve as indicators of the sensitivity and efficiency of our promising thin film device.

The notable advantages of our device include its excellent sensitivity, easy preparation, and cost-effectiveness, making it well-suited for mass production and economic applications in the industrial sector. This breakthrough paves the way for the integration of our optoelectronic device into various industrial applications, offering a viable and practical solution with considerable economic benefits.

2 Experimental section

2.1 Materials

Merck in Germany supplied *m*-methylaniline and hydrochloric acid (HCl), while PioChem in Egypt provided $KMnO_4$ and $K_2S_2O_8$. Sodium hydroxide was obtained from El Naser Chemical Company in Egypt. Additionally, Sigma Aldrich in the USA supplied dimethylformamide and pyrrole.

X-ray powder diffraction (XRD) analysis was conducted using the Bruker D8 XRD instrument, while Fourier-transform infrared spectroscopy (FTIR) analysis utilized the Jasco 340 instrument. Additionally, transmission electron microscopy (TEM) and scanning electron microscopy (SEM) analyses were carried out utilizing the Joel and Hitachi models. Furthermore, optical UV analysis was performed using the PerkinElmer instrument. These distinct instruments were employed for their specialized capabilities in their respective analytical techniques, ensuring comprehensive and precise characterization of the materials under investigation.

2.2 Fabrication of Mn$_2$O$_3$–MnO$_2$–PmMA/Ppy thin film optoelectronic and solar cell device

The synthesis of the Ppy polymer (p-layer) closely follows the methodology established in our previous studies. This involves dissolving the pyrrole monomer (0.06 M) in an acidic medium (0.5 M HCl) and introducing the oxidant (0.15 M K$_2$S$_2$O$_8$) to initiate Ppy formation, resulting in a dark green precipitate [21,22]. Subsequently, the polymer undergoes purification for subsequent analysis.

The Mn$_2$O$_3$–MnO$_2$–PmMA (n-layer) is produced in a similar procedure, albeit with some variations. Here, a stronger oxidizing agent, 0.12 M KMnO$_4$, is used to initiate the oxidation of m-methylaniline. This leads to the generation of free radicals that combine to form PmMA. Notably, KMnO$_4$ serves as an additional source of Mn$_2$O$_3$–MnO$_2$, which becomes integrated into the polymer network. This reaction takes place in a 0.6 M HCl environment, resulting in the creation of a dark green Mn$_2$O$_3$–MnO$_2$–PmMA nanocomposite thin film. Subsequent to the fabrication of these layers, these layers are treated with distilled water and dried at 60°C. Following this process, they are prepared for further characterization procedures.

2.3 Optoelectronic electrical testing

Following the construction of the Mn$_2$O$_3$–MnO$_2$–PmMA/Ppy optoelectronic device, the solar cell behavior is investigated. Both sides of the device undergo coating with Ag-Paste. Electrical testing is then conducted using the CHI608E (USA) with a scanning rate of 100 mV/s, involving the examination of the current–potential relationship under various light conditions, including monochromatic wavelength light. Electrical measurements are conducted under standard room temperature conditions within a voltage range spanning from −2.0 to +2.0 V. During testing, we record both the photogenerated current (J_{ph}) and dark current (J_o) values. These measurements serve as the foundation for deriving further sensitivity and efficiency parameters. Using a metal halide lamp, specifically the vacuum lamp with a power rating of 400 W, in conjunction with optical filters, allows precise control over the energy of light transmitted through the system.

The LDR, D, R, J_{SC}, V_{OC}, and noise ratio are among the key parameters determined from the obtained data. These metrics collectively offer a comprehensive understanding of the solar cell's performance and sensitivity under different illumination conditions.

So, this thorough evaluation provides insights into the device's responsiveness to light, its ability to generate and sustain current under illuminated conditions, and its overall efficiency as a solar cell. The inclusion of monochromatic wavelength light in the testing process ensures a detailed analysis of the device's behavior across specific wavelengths, contributing to a comprehensive understanding of its optoelectronic capabilities.

Efficiency estimation hinges on the utilization of noise ratio parameters, which are contingent upon both the dark current (J_o) and photogenerated current (J_{ph}) factors (referenced as equation (1)). Subsequently, the LDR characterizes the range of input irradiance levels, depicted in decibels (dB), within which the responsivity remains consistent (as illustrated in equation (2)). Similarly, the R values are derived estimates, factoring in the intensity of light (P) (as per equation (3)). Furthermore, the estimation of D incorporates considerations of electron charge (e) and the area of the photodetector, which is standardized at 1.0 cm^2 (delineated in equation (4)). These equations and their accompanying explanations illuminate the intricate interplay between various parameters, facilitating a deeper understanding of the efficiency estimation process.

$$\text{Noise ratio} = \left(\frac{J_o}{J_{ph}}\right) \times 100, \tag{1}$$

$$\text{LDR} = 20\log\left(\frac{J_{ph}}{J_o}\right), \tag{2}$$

$$R = \frac{J_{ph} - J_o}{P}, \tag{3}$$

$$D = R\sqrt{S/2eJ_o}. \tag{4}$$

3 Results and discussion

3.1 Analyses

The chemical structure of P*m*MA is confirmed through the analysis of the FT-IR spectrum, as illustrated in Figure 1. The spectrum exhibits characteristic bands indicative of various functional groups within the polymer. Specifically, the N–H and C–N positions are discerned at 3,410 and 1,370 cm^{-1}, respectively. The presence of the substituent CH$_3$-group is highlighted by the band at 2,928 cm^{-1}, whereas the C=C vibrations of the benzenoid rings appear as bands at 1,498 and 1,529 cm^{-1}. Furthermore, the vibration associated with the quinoid ring is observed at 1,640 cm^{-1}. The C–H in/out-plane vibrations contribute bands at 1,104 and 586 cm^{-1}, respectively.

The functional groups in P*m*MA and Mn$_2$O$_3$–MnO$_2$–P*m*MA exhibit similarities, indicating the retention of key molecular components during the nanocomposite formation. However, the shifts in band positions suggest that the incorporation of Mn$_2$O$_3$–MnO$_2$ introduces alterations in the electronic structure of the nanocomposite. The heightened intensity of the N–H peak, distinctive to the nanocomposite, signifies an augmentation in particle mass throughout its volume. This increase suggests a corresponding enhancement in the crystallinity behavior of the composite when compared to the pure polymer.

The shifts, whether toward the blue or red end of the spectrum, offer insights into the interactions between the inorganic and polymeric components. These shifts are indicative of

Table 1: Positions of the detected functional groups for both P*m*MA and Mn$_2$O$_3$–MnO$_2$–P*m*MA

Band (cm^{-1})		Group
Mn$_2$O$_3$–MnO$_2$–P*m*MA	**P*m*MA**	
3,392	3,410	N–H [23,24]
1,616	1,640	C=C quinone form
1,498	1,529	C=C normal benzene form [25–27]
1,404	1,370	C–N [28]
1,107	1,104	C–H [29]
677	586	Para disubstituted ring [30]

changes in the electron distribution within the polymer matrix, influenced by the presence of Mn$_2$O$_3$–MnO$_2$. A comprehensive summary of these functional groups for both PmMA and Mn$_2$O$_3$–MnO$_2$–P*m*MA is presented in Table 1.

In Figure 1(b), the XRD of the Mn$_2$O$_3$–MnO$_2$–P*m*MA nanocomposite is juxtaposed with that of pure P*m*MA. The pure P*m*MA reveals a non-crystalline nature, evident from the absence of distinct peaks that typify crystalline substances.

Conversely, the XRD pattern of the Mn$_2$O$_3$–MnO$_2$–P*m*MA nanocomposite demonstrates increased crystallinity, revealed by the presence of multiple sharp peaks. These peaks correspond to the existence of βMnO$_2$, an inorganic component, or residual Mn$_2$O$_3$ within the polymer matrix. Specifically, the XRD peaks associated with βMnO$_2$ are positioned at distinct angles,
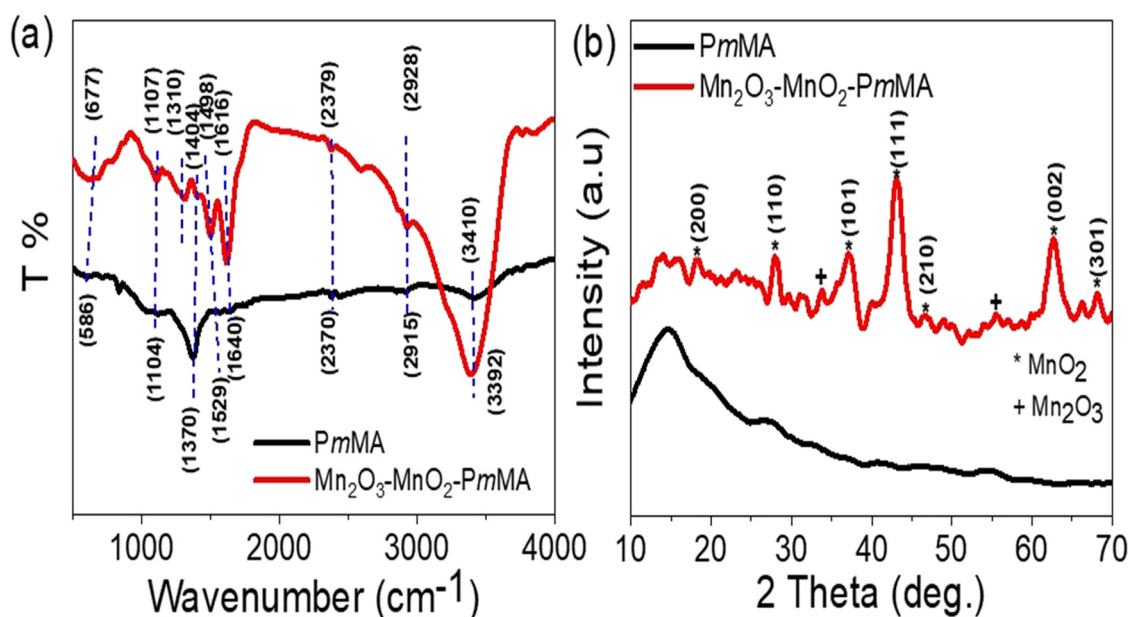

Figure 1: Construction of Mn$_2$O$_3$–MnO$_2$–P*m*MA nanocomposite by (a) FTIR and (b) XRD.

such as 18.1°, 28.2°, 37.2°, 43.1°, 46.9°, 62.7°, and 68.3°, representing various growth orientations. These angles are consistent with the JCPDS 24-0735 reference database [31]. Faint indications XRD peaks of Mn_2O_3 are identifiable at 33.6° and 55.5°. Predominantly, the nanocomposite harbors βMnO_2 as the principal inorganic constituent, interweaving within the polymer matrix and augmenting the composite's structural composition.

By employing equation (5) [32,33], it is possible to approximate the dimensions of the crystalline domains. For the Mn_2O_3–MnO_2–P*m*MA nanocomposite, this calculation yields a crystalline size of 45 nm, offering valuable information about the scale of the crystals within the composite substance.

$$D = 0.9\lambda/W \cos \theta. \qquad (5)$$

XPS is used to verify the elemental composition and oxidation states intrinsic to the synthesized Mn_2O_3–MnO_2–P*m*MA nanocomposite. This analytical tool serves to investigate the inorganic architecture of Mn compounds and their interactions within the polymer framework, P*m*MA. Figure 2(a) depicts the elemental makeup by showing the binding energy for each component. In Figure 2(d)–(f), the pristine polymer,
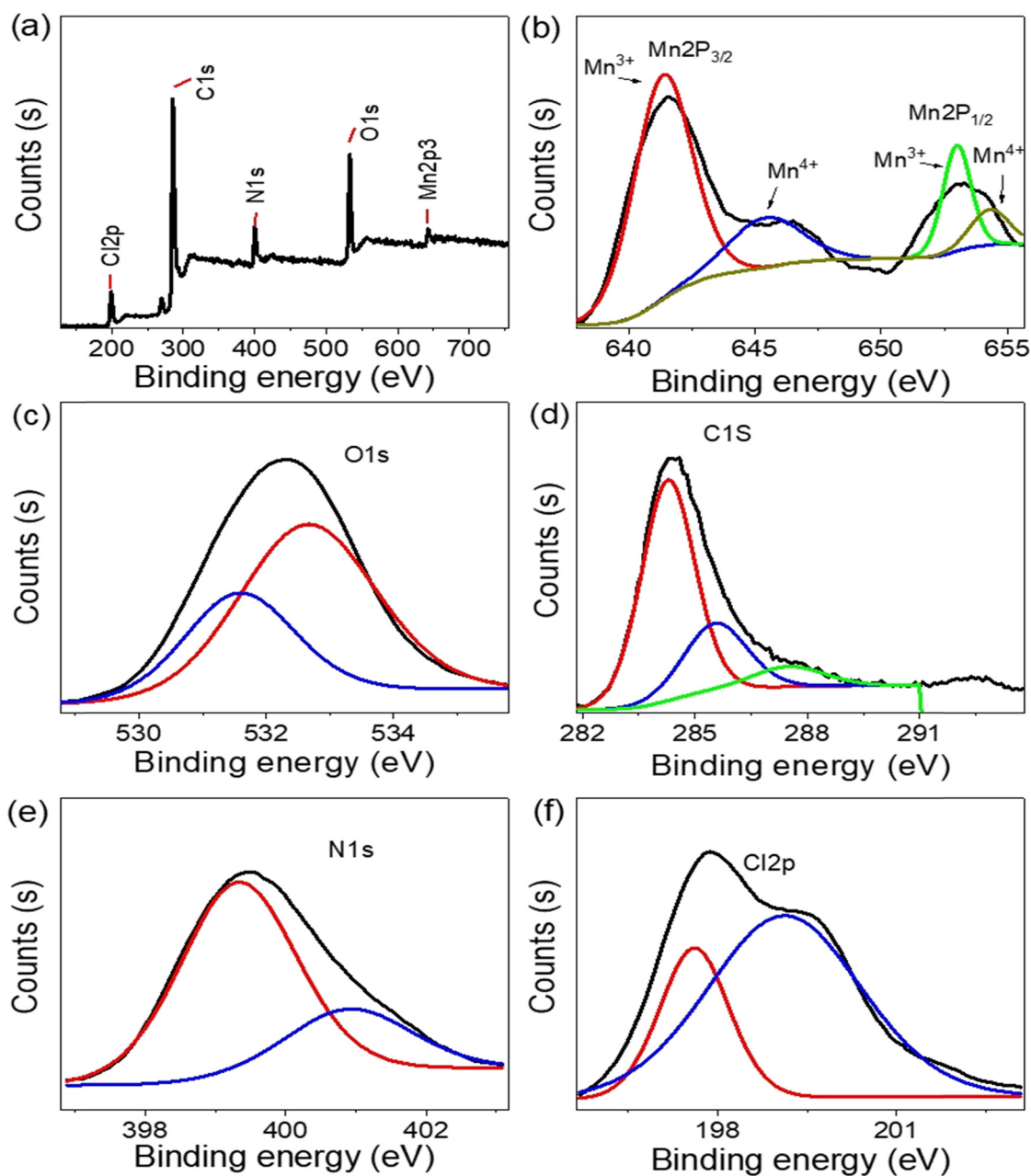

Figure 2: XPS analyses of (a) Mn_2O_3–MnO_2–P*m*MA, (b) Mn, (c) O, (d) C, (e) N, and (f) Cl.
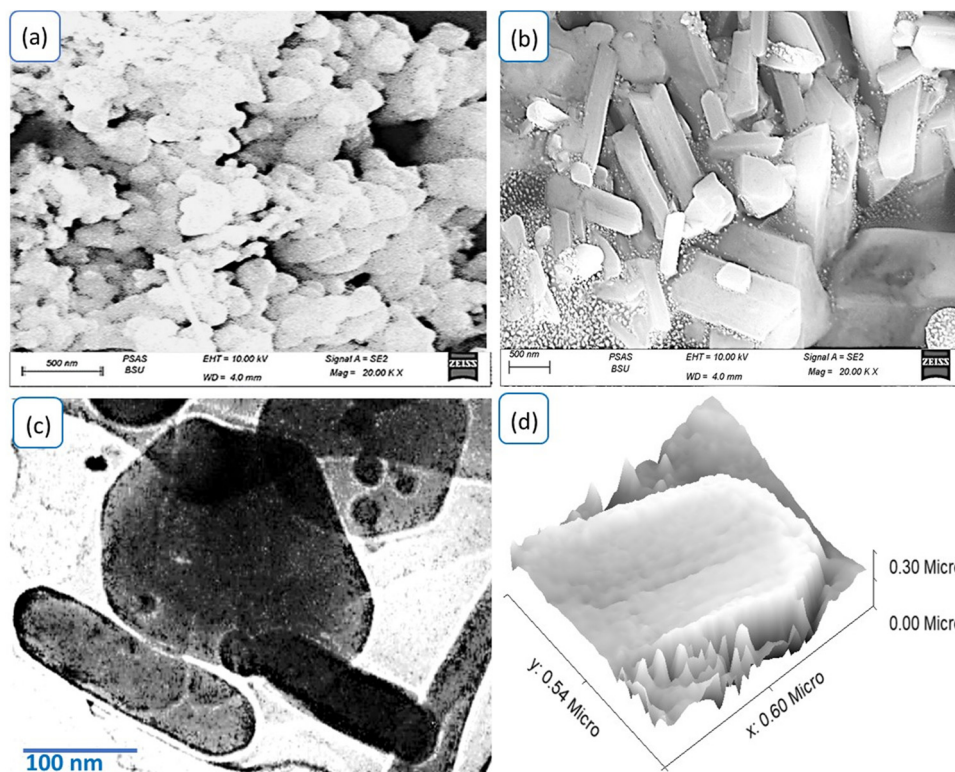
Figure 3: (a) Pure PmMA SEM. The Mn_2O_3–MnO_2–P*m*MA nanocomposite topography and geometric behavior were estimated through the (b) SEM, (c) TEM, and (d) cross-sectional modeling.

P*m*MA, along with constituent elements C, N, and intercalated Cl ions are identified at 285.3, 400.4, and 199.2 eV, respectively. The spectra for Mn, namely $2p_{3/2}$ and $2p_{1/2}$, occupy positions at (641.3 and 645.4 eV) and (653 and 654.4 eV), delineating Mn^{3+} and Mn^{4+} oxidation states [34]. This unequivocally validates the coexistence of Mn_2O_3 and MnO_2 configurations. Furthermore, the O 1s spectrum registers at 533 eV (Figure 2(c)), serving as an additional testament to the compositional intricacies and structural attributes of the nanocomposite.

The Mn_2O_3–MnO_2–P*m*MA nanocomposite exhibits distinct and notable morphological features, prominently showcasing a remarkable nanorod structure that correlates with its precisely defined crystalline properties. This specific structural attribute arises from the incorporation of Mn_2O_3–MnO_2 into the polymer matrix, resulting in a nanocomposite that stands out for its well-defined crystalline nature, as depicted in Figure 3(b).

These nanorods, which constitute the nanocomposite's structure, exhibit varying lengths, spanning from 150 to 1.1 µm, and widths that range between 80 and 300 nm. What distinguishes these nanorods even further is their distinct geometric arrangement, with shapes ranging from hexagonal to pentagonal. This geometric configuration serves as a fundamental factor contributing to the nanocomposite's exceptional optical performance. In sharp contrast, the pure P*m*MA material lacks any discernible geometric arrangement. Instead, it appears as a collection of irregular granules characterized by porous structures that aggregate together, as evident in Figure 3(a).

Further insights into the Mn_2O_3–MnO_2–P*m*MA nanocomposite's structure are provided by the TEM analysis in Figure 3(c), which effectively captures the rod-like geometric nature of the material. A specific rod with dimensions approximately 200 nm in length and 80 nm in width is depicted in this microscopic evaluation. To enhance the verification of this geometric behavior, Figure 3(d) offers a glimpse into the cross-sectional attributes and surface roughness of the fabricated Mn_2O_3–MnO_2–P*m*MA nanorod. This figure notably reinforces the confirmation of the hexagonal shape, aided by the presence of minute particles enveloping the rod's surface. This phenomenon is a consequence of the polymer deposition process. The composition of this potentially effective Mn_2O_3–MnO_2–P*m*MA nanocomposite includes percentages of manganese, oxygen, nitrogen, carbon, and chlorine, estimated at 1.66, 14.02, 8.64, 68.19, and 7.49%, respectively.

So, the morphological analysis of the Mn_2O_3–MnO_2–P*m*MA nanocomposite unveils a striking nanorod structure with distinct geometric shapes, ranging from hexagonal to pentagonal.

This arrangement is in stark contrast to the irregular granular structure observed in pure PmMA. The TEM analysis further substantiates the rod-like nature of the nanocomposite, while the cross-sectional view reinforces the hexagonal shape and the surface features resulting from the polymer deposition process.

The optical characteristics of the Mn$_2$O$_3$–MnO$_2$–PmMA composite nanorods and pure PmMA are assessed through absorbance measurements, as depicted in Figure 4(a). A discernible contrast in optical behavior is evident between these two materials, with the incorporation of Mn$_2$O$_3$–MnO$_2$ inorganic constituents within the polymer filler notably enhancing the optical response. This enhancement is particularly pronounced, extending the absorbance spectrum to around 600 nm, which falls within the middle of the Vis range. In contrast, the pure PmMA exhibits an absorbance spectrum limited to 400 nm, confined to the UV range, with a minor band appearing in the Vis range. The significant integration of Mn$_2$O$_3$–MnO$_2$ with the pure PmMA polymer facilitates pronounced electron transitions between these inorganic materials and the polymer. This integration results in the formation of a singular material exhibiting increased photon absorbance, consequently inducing electron transitions under these photon absorbance conditions. The synergistic effect arising from the combination of these inorganic materials with the pure polymer fosters compatibility in the electron transition process, enhancing overall material performance.

In both the pristine polymer and the nanocomposite, this behavior is attributed to the pi–pi* transition of electrons upon exposure to UV or Vis light. Accumulation of these excited electrons occurs at the polymer surface.

However, in the nanocomposite, these electrons extend their reach to interact with the incorporated inorganic Mn$_2$O$_3$–MnO$_2$ filler. The influence of these inorganic constituents becomes evident in the assessment of the material's bandgap through the Tauc equation (equation (6)) [35,36]. This evaluation reveals a reduction in the bandgap from 2.94 to 2.48 eV, underscoring the impact of the inorganic material integration into the polymer matrix

$$\alpha h\nu = A(h\nu - E_g)^{1/2}. \tag{6}$$

3.2 Electrical study

The investigation of the electrical characteristics of Mn$_2$O$_3$–MnO$_2$–PmMA/Ppy optoelectronic and solar cell devices is undertaken. In this assessment, the Mn$_2$O$_3$–MnO$_2$–PmMA component serves as the n-type material, while Ppy functions as the p-type material. The workstation CHI608E is employed to conduct the evaluation by analyzing the current density and potential relationship at −2.0 to +2.0 V.

The testing protocol involves the use of a metal halide (light source), generating white light for illumination. The light emitted can be finely controlled across various wavelengths using optical filters, enabling the provision of monochromatic lights with distinct energies. During this assessment, the resulting current densities are meticulously examined to derive important parameters such as R (responsivity), LDR and D (detectivity).

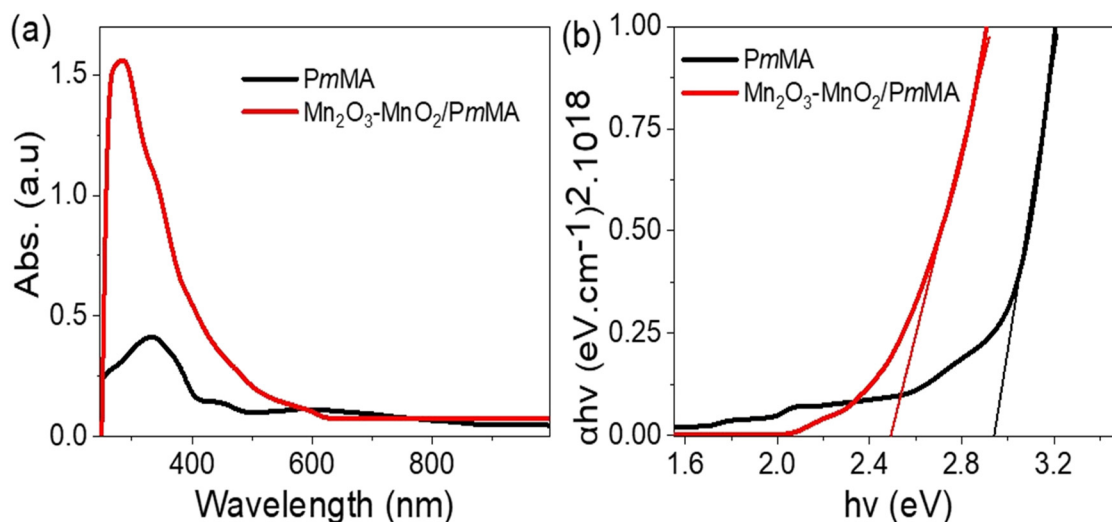In particular, the produced current densities have a great role in the determination of R, LDR, and D, providing

Figure 4: (a) Optical absorbance and (b) the Tauc equation relation for bandgap evaluation for PmMA and Mn$_2$O$_3$–MnO$_2$–PmMA composite nanorods.
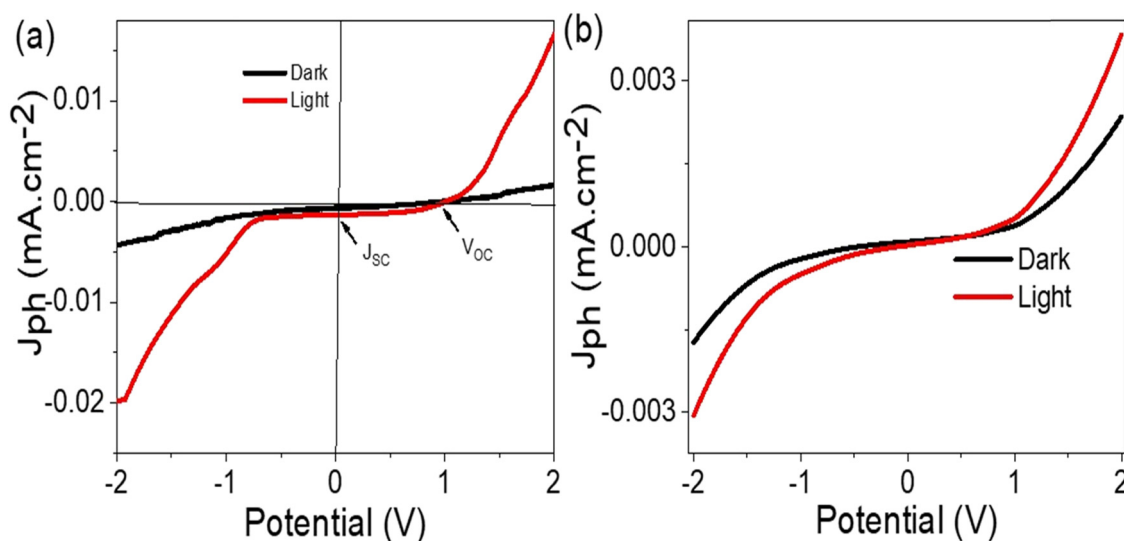
Figure 5: Electrical characteristics of (a) Mn_2O_3–MnO_2–P*m*MA/Ppy optoelectronic and solar cell device under dark and light and (b) of the pristine P*m*MA polymer.

insights into the performance of the Mn_2O_3–MnO_2–P*m*MA/Ppy thin film devices under different conditions. *R* is a reflection of the device's behavior to convert incident light into an electrical signal and is crucial in understanding its efficiency. LDR reveals the sensitivity of the device to light variations. *D* quantifies the ability of the device to detect low optical signals and is an essential parameter for assessing its practical utility.

Additionally, key metrics such as J_{SC} and V_{OC} are integral to understanding the overall behavior of the Mn_2O_3–MnO_2–P*m*MA/Ppy thin film devices. J_{SC} denotes the maximum current generated under short-circuit conditions, representing the device's ability to collect charge carriers efficiently. V_{OC}, the voltage across the device terminals in the absence of current flow, provides insights into the device's photogenerated potential.

This comprehensive evaluation aims to unravel the intricate electrical behavior of the Mn_2O_3–MnO_2–P*m*MA/Ppy thin film devices under various illuminations, facilitating the way for a deeper illustration of their optoelectronic and solar cell functionalities. The systematic analysis of these parameters contributes to the elucidation of the device's performance characteristics, facilitating advancements in the development of efficient and responsive optoelectronic technologies.

The electrical characteristics of Mn_2O_3–MnO_2–P*m*MA/Ppy optoelectronic and solar cell devices are thoroughly explored under both dark and illuminated conditions, with the evaluation focused on the generated J_o (dark current) and J_{ph} (photocurrent) values (Figure 5(a)). The substantial increase in the J_{ph} value compared to J_o confirms

the remarkable responsivity of this material to light, attributed to the efficient generation of hot electrons during electron–hole pair formation within the n-layer, Mn_2O_3–MnO_2–P*m*MA. Meanwhile, the holes readily transfer to the Ppy layer (p-type), resulting in the production of J_{ph} values (0.017 mA cm^{-2}), significantly higher than the J_o value of 0.002 mA cm^{-2}. This substantial improvement underscores the material's enhanced responsiveness to light. Figure 5(b) depicts the electrical characteristics of the fabricated P*m*MA polymer. The constrained J_{ph} and J_o values, measured at −0.003 and −0.001 mA/cm^2, respectively, highlight the restricted electrical performance of this pristine polymer compared to the promising composite comprising Mn_2O_3–MnO_2–P*m*MA.

The LDR is then calculated as 85*D*, a promising value indicating the high sensitivity of the device to changes in light conditions. Additionally, the noise ratio (J_o/J_{ph}) is found to be a minimal 12%, suggesting negligible interference and a high signal-to-noise ratio, further enhancing the device's reliability.

Furthermore, the key parameters J_{SC} and V_{OC} are determined, yielding values of 0.001 mA cm^{-2} and 0.98 V, respectively. While the J_{SC} value is considered satisfactory, the V_{OC} value is particularly promising. The substantial open-circuit voltage indicates the device's capability to maintain a high voltage across its terminals even when no current is flowing, which is crucial for efficient power conversion in solar cells. This promising V_{OC} value suggests the potential of the Mn_2O_3–MnO_2–P*m*MA/Ppy thin film device for effective solar energy conversion.

So, the comprehensive evaluation of the electrical behavior of these optoelectronic and solar cell devices

reveals their exceptional performance under both dark and illuminated conditions. The increased photocurrent, coupled with favorable LDR and noise ratio values, signifies the material's great potential for light-sensing applications. The calculated J_{SC} and V_{OC} values further underscore the promising attributes of the device, positioning it as a viable candidate for efficient solar energy harvesting.

The Mn_2O_3–MnO_2–P*m*MA/Ppy thin film optoelectronic device's response to controlled monochromatic wavelengths, achieved through optical filters at 340, 440, 540, and 730 nm, is shown in Figure 6(a) and (b). The device has a remarkable sensitivity to UV light, evidenced by the optimal J_{ph} value of -0.021 mA cm^{-2} at -2.0 V. This exceptional behavior aligns with the optical absorbance curve depicted in Figure 4(a), confirming the device's heightened responsiveness in the UV region. The high energy of UV light facilitates the efficiency of electron collection to the conducting band, generating free electrons capable of surface movement, ultimately resulting in the observed J_{ph} value. The calculated energy for photons with a wavelength of 340 nm, based on the equation ($E = hv$), is 3.8 eV – an energy surpassing the bandgap value of 2.48 eV (Figure 4(b)).

Furthermore, the optoelectronic device has a response in the Vis region, yielding a J_{ph} value of -0.009 mA cm^{-2} at -2.0 V. This response is attributed to the behavior of the device in the Vis region, where the energy of photons is 2.8 eV, surpassing the bandgap value (Figure 4(b)). Notably, the response is particularly evident for photons at 540 nm (Vis region), with a generated J_{ph} of -0.007 mA/cm^2 at -2.0 V.

As the energy of photons decreases to 1.8 eV at 730 nm, falling below the bandgap value of 2.48 eV, the optical region encounters limitations. In this scenario, the reduced photon energy is insufficient for facilitating the transfer of hot electrons. Consequently, the J_{ph} value closely approximates the J_o value observed in the dark, indicating that the optoelectronic device is unable to operate effectively within this specific optical region (-0.005 mA/cm^2). The inadequacy of photon energy to induce the transfer of hot electrons underscores the device's dependency on sufficient energy levels for its functionality. The optical limitations in this spectral range impede the generation of photocurrent, emphasizing the critical role of matching photon energy to the bandgap for the efficient operation of the Mn_2O_3–MnO_2–P*m*MA/Ppy thin film optoelectronic device. This understanding of the device's response across different optical regions is crucial for optimizing its performance and guiding its application in areas where specific energy levels are requisite for effective optoelectronic processes.

The assessment of the efficiency of the Mn_2O_3–MnO_2–P*m*MA/Ppy optoelectronic and solar cells encompasses a comprehensive exploration under diverse monochromatic wavelengths, unveiling the distinct sensitivities of this thin film. The parameters R and D are crucial in this evaluation, determined by equations (3) and (4), respectively [37]. These equations gauge the thin film devices' performance in converting photons into detectable hot electrons. Figure 7(a) and (b) show the variation of R and D values across different wavelengths.

The analysis reveals that the optimal R and D values at 340 nm, attaining 0.22 mA W^{-1} and 0.47×10^8 Jones, respectively. Even at 540 nm, where these values decrease to 0.08 and 0.2×10^8 Jones, they remain relatively high, indicating
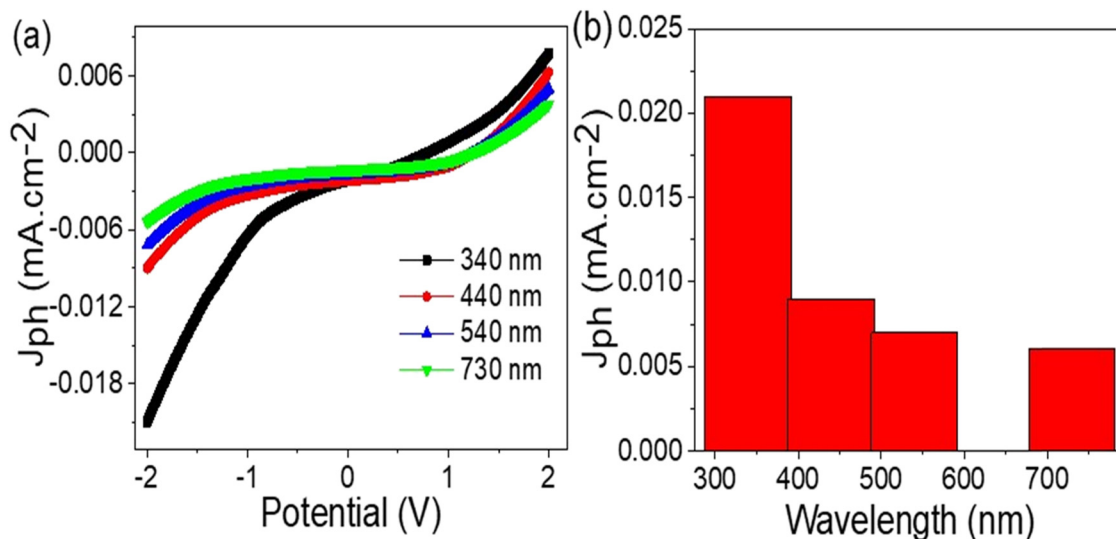

Figure 6: Electrical characteristics of Mn_2O_3–MnO_2–P*m*MA/Ppy optoelectronic and solar cell devices under various monochromatic light through (a) current density–potential relationship and (b) the J_{ph} values at -2.0 V.
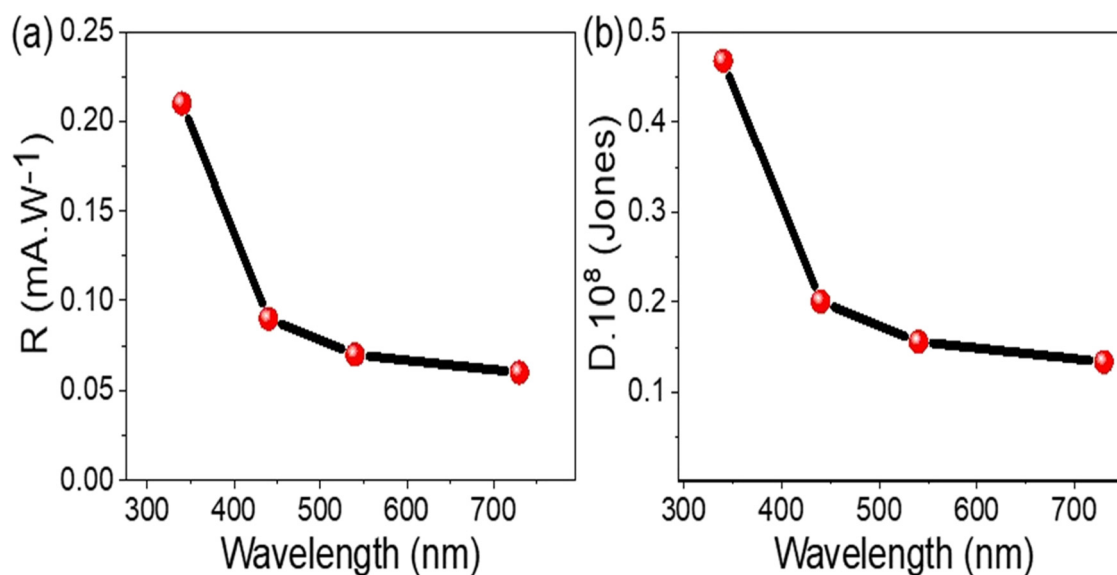
Figure 7: Efficiency performance of Mn_2O_3–MnO_2–P*m*MA/Ppy optoelectronic and solar cell devices under various monochromatic photons by (a) *R* and (b) *D* values.

robust photon conversion to hot electrons. This versatility in response to various optical regions positions the thin film device as a promising candidate for optoelectrical applications in the industrial sector, particularly in light sensing.

Furthermore, this opens up possibilities for the synthesis of thin-film solar cells utilizing the thin-film technique. The utilization of two layers of polymer materials in the fabrication process enhances cost-effectiveness. The notable

performance of the device in converting photons to hot electrons underscores its potential for thin-film solar cell applications, contributing to the advancement of economical and efficient photovoltaic technologies.

In comparison with previous studies, the outcomes of this investigation, detailed in Table 2, underscore the favorable behavior of the Mn_2O_3–MnO_2–P*m*MA/Ppy thin film in optoelectronic applications. The robust *R* and *D* values, coupled with the device's response across varied optical

Table 2: Evaluated efficiency of the fabricated Mn_2O_3–MnO_2–P*m*MA/Ppy thin film optoelectronic and solar cell device through the *R*-value calculation

Structure	Wavelength (nm)	Bais (V)	*R* (mA W^{-1})
Ti_3C_2 MXenes [13]	405	5	0.07
ZnO/P3HT/PEDOT:PSS [16]	365	2	0.1
PBBTPD: Tri-PC$_{61}$BM [15]	350	5	10^{-4}
PbI_2-5%Ag [12]	532	6	NA
TiN/TiO_2 [11]	550	5	—
CuO nanowires [9]	390	5	—
GaN-graphene [10]	365	7	0.003
Graphene-PbI_2 [38]	550	2	NA
P3HT [14]	325	1	NA
ZnO/RGO [39]	350	5	1.3×10^{-3}
Se/TiO_2[40]	450	1	5×10^{-3}
GO/Cu_2O [41]	300	2	0.5×10^{-3}
ZnO-CuO [42]	405	1	3×10^{-3}
ZnO/Cu_2O [43]	350	2	4×10^{-3}
TiO_2-PANI [44]	320	0	3×10^{-3}
CuO/Si [45]	405	0.2	0.003
PC$_{71}$BM [46]	300	2	0.005
Mn_2O_3–MnO_2–P*m*MA/Ppy optoelectronic (this work)	340	2	0.22

regions, reinforce its potential for industrial implementation and highlight its superiority in comparison to alternative studies.

In conclusion, this study not only elucidates the efficient performance of the Mn_2O_3–MnO_2–P*m*MA/Ppy thin film in optoelectronic and solar cell applications but also positions it as a promising and cost-effective candidate for industrial utilization. The findings have great insights into the thin film's behavior across different wavelengths, paving the way for achieving optoelectronics and thin-film solar cell technologies.

4 Conclusions

Utilizing a one-pot synthesis method, a composite nanorod structure consisting of Mn_2O_3–MnO_2–P*m*MA (n-layer) on a Ppy film (p-layer) was created and tested electrically as optoelectronic and solar cell thin film devices. The optical features of the n-layer, combined with the nanorods' morphological behavior, enhance optical absorbance efficiency, resulting in a reduced bandgap value of 2.48 eV. The n-type Mn_2O_3–MnO_2–P*m*MA composite is evaluated with a crystalline size of 45 nm. These nanorods, which constitute the nanocomposite's structure, exhibit varying lengths, spanning from 150 to 1.1 μm, and widths that range between 80 and 300 nm. The primary determinant of the optoelectronic device's performance is the notably higher photocurrent density (J_{ph}) value of 0.017 mA/cm^2 in comparison to the J_o of 0.002 mA/cm^2. Furthermore, the LDR is 85%, and the noise ratio is 12%. The optimized values for photosensitivity (R) and detectivity (D) at 340 nm are achieved at 0.22 mA W^{-1} and 0.47 × 10^8 Jones, correspondingly. Even at 540 nm, these values decrease to 0.08 and 0.2 × 10^8 Jones, respectively. Regarding solar cell behavior, the J_{SC} and V_{OC} at 540 nm are determined, yielding values of 0.001 mA/cm^2 and 0.98 V, respectively. The exceptional performance of this optoelectronic device, along with its solar cell characteristics, positions the thin film material for a dual role in various industrial applications.

Author contributions: Mohamed Rabia: Experimental, writing, and analysis; Eman Aldosari: Writing, analysis, and Funding; Hassan A. Ewais and Kenan Song: Supervision and revising.

References

[1] Wang Q, Ma X, Wu P, Li B, Zhang L, Shi J. CoNiFe-LDHs decorated Ta3N5 nanotube array photoanode for remarkably enhanced photoelectrochemical glycerol conversion coupled with hydrogen generation. Nano Energy. 2021;89:106326.

[2] Petrakopoulou F, García-Tenorio E. Evaluating hydrogen-based electricity generation using the concept of total efficiency. Energy Convers Manag. 2023;293:117438.

[3] Sharma R, Almáši M, Punia RC, Chaudhary R, Nehra SP, Dhaka MS, et al. Solar-driven polymer electrolyte membrane fuel cell for photovoltaic hydrogen production. Int J Hydrog Energy. 2023;48:37999–8014.

[4] Meda US, Rajyaguru YV, Pandey A. Generation of green hydrogen using self-sustained regenerative fuel cells: Opportunities and challenges. Int J Hydrog Energy. 2023;48:28289–314.

[5] Su N. Improving electrical conductivity, thermal stability, and solubility of polyaniline-polypyrrole nanocomposite by doping with anionic spherical polyelectrolyte brushes. Nanoscale Res Lett. 2015;10:1–9.

[6] Castillo-Ortega MM, Santos-Sauceda I, Encinas JC, Rodriguez-Felix DE, Castillo-Castro T, Rodriguez-Felix F, et al. Adsorption and desorption of a gold-iodide complex onto cellulose acetate membrane coated with polyaniline or polypyrrole: A comparative study. J Mater Sci. 2011;46:7466–74.

[7] Rabia M, Elsayed AM, Alnuwaiser MA. Preparation and characterization of polyhedron Mn(III) Oxide/-β-Mn(IV) oxide/poly-o-chloroaniline porous nanocomposite for electroanalytical photon detection processes. 2023;11:2375.

[8] Rabia M, Shaban M, Jibali BM, Abdelkhaliek AA. Effect of Annealing Temperature on the Photoactivity of ITO/VO 2 (M)/Au Film Electrodes for Water Splitting. J Nanosci Nanotechnol. 2020;20:4120–30.

[9] Wang SB, Hsiao CH, Chang SJ, Lam KT, Wen KH, Hung SC, et al. A CuO nanowire infrared photodetector. Sens Actuators A: Phys. 2011;171:207–11.

[10] Kalra A, Vura S, Rathkanthiwar S, Muralidharan R, Raghavan S, Nath DN. Demonstration of high-responsivity epitaxial β-Ga2O3/GaN metal-heterojunction-metal broadband UV-A/UV-C detector. Appl Phys Express. 2018;11:064101.

[11] Naldoni A, Guler U, Wang Z, Marelli M, Malara F, Meng X, et al. Broadband Hot-Electron Collection for Solar Water Splitting with Plasmonic Titanium Nitride. Adv Opt Mater. 2017;5:1601031.

[12] Ismail RA, Mousa AM, Shaker SS. Visible-enhanced silver-doped PbI2 nanostructure/Si heterojunction photodetector: effect of doping concentration on photodetector parameters. Opt Quantum Electron. 2019;51:1–19.

[13] Sreedhar A, Ta QTH, Noh JS. Versatile role of 2D Ti3C2 MXenes for advancements in the photodetector performance: A review. J Ind Eng Chem. 2023;127:1–17.

[14] Tan WC, Shih WH, Chen YF. A highly sensitive graphene-organic hybrid photodetector with a piezoelectric substrate. Adv Funct Mater. 2014;24:6818–25.

[15] Zheng L, Zhu T, Xu W, Liu L, Zheng J, Gong X, et al. Solution-processed broadband polymer photodetectors with a spectral response of up to 2.5 μm by a low bandgap donor–acceptor conjugated copolymer. J Mater Chem C. 2018;6:3634–41.

[16] Ouyang B, Zhang K, Yang Y. Self-powered UV photodetector array based on P3HT/ZnO nanowire array heterojunction. Adv Mater Technol. 2017;2:1700208.

[17] Shaban M, Rabia M, Fathallah W, El-Mawgoud NA, Mahmoud A, Hussien H, et al. Preparation and characterization of polyaniline and Ag/polyaniline composite nanoporous particles and their antimicrobial activities. J Polym Environ. 2018;26:434–42.

[18] Rabia M, Mohamed HSH, Shaban M, Taha S. Preparation of polyaniline/PbS core-shell nano/microcomposite and its application for photocatalytic H2 electrogeneration from H₂O. Sci Rep. 2018;8:1107.

[19] Al-Harbi N, Atta A, Henaish AMA, Rabia M, Abdelhamied MM. Structural, characterization, and linear/nonlinear optical behavior of polyaniline/cellulose acetate composite films. J Mater Sci: Mater Electron. 2023;34:1–14.

[20] Sendi RK, Atta A, Al-Harbi N, Rabia M, Abdelhamied MM. Structural investigation and optical characteristics of low-energy hydrogen beam irradiated polyvinyl alcohol/polyaniline composite materials. Opt Quantum Electron. 2023;55:1–19.

[21] Elsayed AM, Abdallah Alnuwaiser M, Rabia M. Effect of brain-like shape polypyrrole nanomaterial on the capacitance and stability enhancements of β-Ni(OH)2 two-symmetric electrodes supercapacitor. J Mater Science: Mater Electron. 2023;34:1–10.

[22] Trabelsi ABG, Elsayed AM, Alkallas FH, AlFaify S, Shkir M, Alrebdi TA, et al. Photodetector-based material from a highly sensitive freestanding graphene oxide/polypyrrole nanocomposite. Coat 2023. 2023;13:1198.

[23] Siddique AB, Amr D, Abbas A, Zohra L, Irfan MI, Alhoshani A, et al. Synthesis of hydroxyethylcellulose phthalate-modified silver nanoparticles and their multifunctional applications as an efficient antibacterial, photocatalytic and mercury-selective sensing agent. Int J Biol Macromol. 2024;256:128009.

[24] Ullah S, Khalid R, Rehman MF, Irfan MI, Abbas A, Alhoshani A, et al. Biosynthesis of phyto-functionalized silver nanoparticles using olive fruit extract and evaluation of their antibacterial and antioxidant properties. Front Chem. 2023;11:1202252.

[25] Sayyah SM, Shaban M, Rabia M. A high-sensitivity potentiometric mercuric ion sensor based on m-toluidine films. IEEE Sens J. 2016;16:1541–8.

[26] Assad N, Naeem-ul-Hassan M, Ajaz Hussain M, Abbas A, Sher M, Muhammad G, et al. Diffused sunlight assisted green synthesis of silver nanoparticles using Cotoneaster nummularia polar extract for antimicrobial and wound healing applications. Nat Product Res. 2023;6:1–15.

[27] Ejaz A, Mamtaz Z, Yasmin I, Shaban M, Siddique AB, Irfan MI, et al. Cyperus scariosus extract based greenly synthesized gold nanoparticles as colorimetric nanoprobe for Ni2 + detection and as antibacterial and photocatalytic agent. J Mol Liq. 2024;393:123622.

[28] Sayyah SM, Shaban M, Rabia M. M-toluidine polymer film coated platinum electrode as a pH sensor by potentiometric methods. Sens Lett. 2015;13:961–6.

[29] Sayyah SM, Shaban M, Rabia M. Electropolymerization of *m*-toluidin on platinum electrode from aqueous acidic solution and character of the obtained polymer. Adv Polym Technol. 2018;37:126–36.

[30] Sayyah E-SM, Shaban M, Rabia M. A sensor of *m*-cresol nanopolymer/Pt-electrode film for detection of lead ions by potentiometric methods. Adv Polym Technol. 2018;37:1296–304.

[31] Shi K, Luo M, Ying J, Zhen S, Xing Z, Chen R. Extraction of lithium from single-crystalline lithium manganese oxide nanotubes using ammonium peroxodisulfate. iScience. 2020;23:101768.

[32] Rajeevgandhi C, Sathiyamurthy K, Guganathan L, Savithiri S, Bharanidharan S, Mohan K. Experimental and theoretical investigations on the spinel structure of Co2O3 nanoparticles synthesized via simple co-precipitation method. J Mater Sci: Mater Electron. 2020;31:16769–79.

[33] Noori SM. Synthesis and characterization of Ni-Si 3 N 4 nanocomposite coatings fabricated by pulse electrodeposition. Bull Mater Sci. 2034;42:44.

[34] Wang M, Chen K, Liu J, He Q, Li G, Li F. Efficiently enhancing electrocatalytic activity of α-MnO2 nanorods/N-doped ketjenblack carbon for oxygen reduction reaction and oxygen evolution reaction using facile regulated hydrothermal treatment. Catalysts. 2018;8.

[35] Haryński Ł, Olejnik A, Grochowska K, Siuzdak K. A facile method for Tauc exponent and corresponding electronic transitions determination in semiconductors directly from UV–Vis spectroscopy data. Opt Mater. 2022;127:112205.

[36] Aziz SB, Nofal MM, Ghareeb HO, Dannoun EMA, Hussen SA, Hadi JM, et al. Characteristics of poly(vinyl Alcohol) (PVA) based composites integrated with green synthesized Al3 + -metal complex: structural, optical, and localized density of state analysis . *Polymers*. 2021;13:1316.

[37] Awad MA, Shaban M, Rabia M. The efficiency of M (M = Li, Na, or Cs) doped CdS nanomaterials in optoelectronic applications. Int J Energy Res. 2022;46:8443–51.

[38] Chen Z, Ci H, Tan Z, Dou Z, Chen X-D, Liu B, et al. Growth of 12-inch uniform monolayer graphene film on molten glass and its application in PbI 2-based photodetector. Nano Res. 2019;12:1888–93.

[39] Liu K, Sakurai M, Liao M, Aono M. Giant improvement of the performance of ZnO nanowire photodetectors by Au nanoparticles. J Phys Chem C. 2010;114:19835–9.

[40] Zheng L, Hu K, Teng F, Fang X. Novel uv–visible photodetector in photovoltaic mode with fast response and ultrahigh photosensitivity employing Se/TiO2 Nanotubes heterojunction. Small. 2017;13.

[41] Lan T, Fallatah A, Suiter E, Padalkar S. Size controlled copper (I) oxide nanoparticles influence sensitivity of glucose biosensor. Sensors. 2017;17:1944.

[42] Costas A, Florica C, Preda N, Apostol N, Kuncser A, Nitescu A, et al. Radial heterojunction based on single ZnO-CuxO core-shell nanowire for photodetector applications. Sci Rep. 2019;9:1–9.

[43] Bai Z, Zhang Y. Self-powered UV–visible photodetectors based on ZnO/Cu2O nanowire/electrolyte heterojunctions. J Alloy Compd. 2016;675:325–30.

[44] Zheng L, Yu P, Hu K, Teng F, Chen H, Fang X. Scalable-production, self-powered TiO₂ nanowell-organic hybrid UV photodetectors with tunable performances. ACS Appl Mater Interfaces. 2016;8:33924–32.

[45] Hong Q, Cao Y, Xu J, Lu H, He J, Sun JL. Self-powered ultrafast broadband photodetector based on p-n heterojunctions of CuO/Si nanowire array. ACS Appl Mater Interfaces. 2014;6:20887–94.

[46] Qi J, Han J, Zhou X, Yang D, Zhang J, Qiao W, et al. Optimization of broad-response and high-detectivity polymer photodetectors by bandgap engineering of weak donor-strong acceptor polymers. Macromolecules. 2015;48:3941–8.